

Synthesis, structure, and magnetic characterization of $\text{La}_{2-x}\text{R}_x\text{RuO}_5$ ($R = \text{Pr, Nd, Sm, Gd, Dy}$)

S. Riegg*

Experimental Physics V, Center for Electronic Correlations and Magnetism, University of Augsburg, D-86135 Augsburg, Germany

U. Sazama and M. Fröba

Inorganic and Applied Chemistry, University of Hamburg, D-20146 Hamburg, Germany

A. Reller

Resource Strategy, University of Augsburg, D-86135 Augsburg, Germany

S. G. Ebbinghaus

Solid State Chemistry, Martin-Luther-University Halle-Wittenberg, D-06099 Halle, Germany

(Received 8 April 2011; revised manuscript received 25 May 2011; published 18 July 2011)

Polycrystalline samples of $\text{La}_{2-x}\text{R}_x\text{RuO}_5$ ($R = \text{Pr, Nd, Sm, Gd, Dy}$) have been prepared, applying a soft-chemistry route based on the thermal decomposition of citric acid precursors. By powder x-ray and neutron diffraction the crystal structures have been investigated in detail. For the unsubstituted parent compound La_2RuO_5 , synchrotron x-ray diffraction patterns reveal a broad structural phase transition regime around 170 K without any significant hysteresis. This structural transition is linked with a drastic reduction of the magnetic susceptibility. A similar behavior was also observed for the lanthanide-substituted compounds $\text{La}_{2-x}\text{R}_x\text{RuO}_5$. Magnetic measurements reveal the coexistence of two weakly interacting magnetic sublattices. The effect of rare-earth substitution on the magnetic phase transition is resulting from structural modifications caused by the smaller radius of the R^{3+} ions. These ions are predominantly located within the LaO-layers, which are alternating with LaRuO_4 layers. The transition temperatures determined by differential scanning calorimetry (DSC) are compared to data derived from the susceptibility measurements.

DOI: [10.1103/PhysRevB.84.014403](https://doi.org/10.1103/PhysRevB.84.014403)

PACS number(s): 75.30.Kz, 61.50.Ks, 65.40.G–, 81.20.Fw

I. INTRODUCTION

The close interaction of chemical composition, crystal structure, and physical properties is a characteristic feature of perovskite-type oxides. Often dramatic variations of the physical properties are caused by very slight (temperature-dependent) changes in the crystal structure. The corresponding transition temperatures are in many cases strongly affected by even small modifications of the chemical composition.

The layered ruthenate La_2RuO_5 shows a phase transition at roughly 170 K, which affects structure, magnetic properties, and electric conductivity.^{1–3} The crystal structure of La_2RuO_5 can be described by LaRuO_4 -zigzag layers of corner-sharing RuO_6 octahedra (similar to the structural motive of, for example, LaTaO_4) separated by LaO layers¹ as shown in Fig. 1. The high-temperature (ht-) phase of La_2RuO_5 is characterized by a monoclinic crystal structure ($P2_1/c$), a paramagnetic behavior in accordance with the $S = 1$ moments of the Ru^{4+} ions, and a band gap of roughly 0.15 eV. In contrast, the low-temperature (lt-) phase possesses a triclinic symmetry ($P1$), the total magnetic moment is strongly reduced and the band gap increases to 0.21 eV.² These findings were originally explained with an orbital-ordering effect.^{4,5} Density-functional-theory (DFT) calculations later revealed a spin-Peierls-like situation in the lt phase where Ru dimers are formed during the structural change. In addition, the DFT calculations also indicated a second perpendicular ordering, leading to the formation of a spin ladder.^{6,7} More recent muon-spin-rotation studies supported the existence of $S = 1$ in the lt-phase.⁸

The coexistence of the structural phase transition and the magnetic ordering raises the question whether the structural changes are the origin or the result of the magnetic interaction. To address this question, we partly substituted La^{3+} by other rare-earth ions. Since these are smaller in size and carry magnetic moments of different magnitudes, we expected these ions to strongly affect the structural-transition temperatures (by stress) and/or the magnetic coupling (by introducing additional interactions).

While the undoped compound has been comparatively well examined, little is known about substituted La_2RuO_5 . To the best of our knowledge, there is only a short note on Pr-substituted La_2RuO_5 in literature.³ Due to the decreasing ionic radii of the lanthanides, rare-earth substitutions should result in a reduction of the interatomic distances. It is expected that the smaller Ru-Ru distance increases the magnetic interaction resulting in higher transition temperatures. In addition, the interaction of the magnetic moments of the lanthanides with the magnetic coupling of the Ru-spin moments has to be regarded. In this context, also the distribution of the rare-earth ions in the crystal structure has to be taken into account. Because of their closer proximity, an additional magnetic moment in the LaRuO_4 layers may have a stronger impact on the magnetic transition than a substitution, which takes place mainly in the LaO layers. Another point that has to be considered is the magnitude of the magnetic moment of the different rare-earth ions. If an interaction exists, a high magnetic moment, e.g., for Gd^{3+} or Dy^{3+} , should affect the ordering more than a very small moment, e.g., for Sm^{3+} . As will be shown in this paper, the influence of the rare-earth's

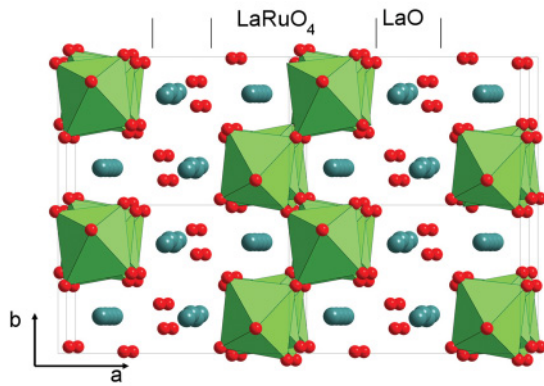


FIG. 1. (Color online) Crystal structure of La_2RuO_5 ($2 \times 2 \times 2$ unit cells) viewed perpendicular to the ab plane and almost along the c axis. La is represented by dark green spheres, oxygen by red spheres, and the RuO_6 octahedra are drawn in light green. The alternating LaO and LaRuO_4 layers along the a axis are indicated at the top of the figure.

moments is very small while their sizes have a pronounced effect.

A full substitution of the diamagnetic La^{3+} ions by other rare-earth ions (Pr, Nd, Sm, Gd, and Dy) leads to the sum formula $R_2\text{RuO}_5$. Some of these compounds have actually been prepared in the absence of oxygen from the binary oxides.^{9–11} However, the $R_2\text{RuO}_5$ oxides crystallize in a completely different orthorhombic structure, which is isostructural to Y_2TiO_5 .¹² In an oxygen-containing atmosphere, the smaller lanthanides are known to form ruthenate-pyrochlores ($R_2\text{Ru}_2\text{O}_7$).^{13,14} For this reason, a complete substitution was not achieved in this work, but a partial replacement of La was successfully carried out up to a certain maximum substitution level at which the structure becomes unstable. First attempts to prepare rare-earth-substituted samples by classical solid-state synthesis were not successful. No single-phase compounds could be obtained, instead the reaction products contained significant amounts of pyrochlore impurities. Thus a soft-chemistry-synthesis method based on the thermal decomposition of citric-acid-stabilized precursors¹⁵ has been developed to prepare single-phase powder samples.

The obtained $\text{La}_{2-x}R_x\text{RuO}_5$ samples were investigated with respect to their crystal structure (powder x-ray, synchrotron, and neutron diffraction) and magnetic properties. Moreover, the phase transition temperature was determined from differential scanning calorimetry (DSC) and compared to values derived from magnetic-susceptibility data. A first brief overview of the Pr samples has already been published.¹⁶

II. EXPERIMENT

Polycrystalline samples of $\text{La}_{2-x}R_x\text{RuO}_5$ were prepared by a soft-chemistry synthesis route similar to the Pechini¹⁷ method. The process starts with a solution of the rare-earth nitrates [$\text{La}(\text{NO}_3)_3 \times 6\text{H}_2\text{O}$ (Fluka 99.9%), $\text{Pr}(\text{NO}_3)_3 \times 5.7\text{H}_2\text{O}$ (Chempur 99.9%), $\text{Nd}(\text{NO}_3)_3 \times 5.8\text{H}_2\text{O}$ (Aldrich 99.9%), $\text{Sm}(\text{NO}_3)_3 \times 5.4\text{H}_2\text{O}$ (Merck), $\text{Gd}(\text{NO}_3)_3 \times 6\text{H}_2\text{O}$ (Aldrich 99.9%), and $\text{Dy}(\text{NO}_3)_3 \times 5.34\text{H}_2\text{O}$ (Alfa Aesar 99.9%)], rutheniumacetylacetonate (Ru-acac) (Chempur 99.9%, Ru

content between 22.5 and 22.9%), and citric acid. The water contents of the nitrates were determined by thermogravimetric measurements using a TA Instruments Q500 thermobalance. The weights of the starting reagents were calculated to obtain 0.75 g of the final oxide. For each mole of metal cations three moles of citric acid were used. First, the nitrates and the Ru-acac were dissolved in approximately 75 ml of ethanol (96%) at room temperature. Afterwards the citric acid was added. The solutions were heated to 90 °C for four hours under stirring until gels formed. These gels were prereacted at 180 °C for two hours and afterwards fully pyrolyzed at 600 °C for 12 hours. The obtained amorphous powders were well ground using agate mortar and pestle and calcined for at least 96 hours at 1175 °C with intermediate grindings every 48 hours. After each of the calcination steps, phase purity was checked by x-ray powder diffraction.

For Rietveld structure analysis,¹⁸ $\Theta - 2\Theta$ scans in the angular range 10°–150° were performed at room temperature on a Seifert XRD TT 3003 diffractometer (Cu- $K_{\alpha 1,2}$ radiation) equipped with secondary monochromator and scintillation counter. A step width of 0.02° and a counting time of 10 s per data point were applied. During the course of this work, the diffractometer was upgraded with a one-dimensional single-line semiconductor detector (Meteor 1D). With this detector a step width of 0.01° and an integration time of 300 seconds were used. Data sets that were recorded with the classical scintillation counter are marked with an asterisk in the table of the supplementary information.¹⁹ The structure analysis was carried out with the Fullprof suite.²⁰ The refinement of the ruthenium- and oxygen-site occupancies lead to values very close to unity, therefore they are not listed explicitly in the tables in the supplementary. The La/R site occupancies were set to the nominal value since the x-ray atomic form factors are almost identical.

Low-temperature x-ray diffraction (Cu- $K_{\alpha 1,2}$ radiation) was performed on a Philips XPert diffractometer using an Anton Paar TTK 450 camera. The sample-holder cavity of approximately $14 \times 10 \times 1 \text{ mm}^3$ was filled with a mixture of oxide powder and Zapon varnish. The varnish improves the thermal conductivity between the sample and the sample holder, which is cooled by flowing cold nitrogen gas. The sample temperature was calibrated by studying the unit-cell volume of zinc powder. For this, the zinc x-ray pattern was measured at different temperatures and the volume change was compared to the known expansion factor of $83.3 \times 10^6 \text{ K}^{-1}$.²¹ A deviation of about 5 to 10 K between the set point and the actual sample temperature was observed. The samples were measured at the (corrected) temperature of 128 K in an angle range from 10° to 100° 2Θ in 0.02° steps and an integration time of 5 seconds per data point.

Neutron-diffraction patterns were measured at the HRPT diffractometer of SINQ at the Paul Scherrer Institute, Switzerland,²² at 1.5 and 300 K. A wavelength of 1.494 Å (Ge 311 monochromator) and a step width of 0.05° were chosen. The measured angle range was 8° to 164° 2Θ .

Synchrotron radiation x-ray diffraction patterns were recorded at beamline B2 (see Ref. 23) at HASYLAB between 50 K and room temperature in approximately 10 K intervals. The powder sample was glued on Capton foil and measured in transmission mode using a wavelength of 0.499309 Å (Si 311)

with a step width of 0.004° over a 2Θ range from 2° to 75° . The data were recorded with the on-site readable position-sensitive image-plate detector (OBI, see Ref. 24) using an integration time of 180 seconds. Again, Rietveld analysis was carried out with the Fullprof suite.

Magnetic properties were investigated on a Quantum Design MPMS 5 SQUID magnetometer in the temperature range from 2 to 400 K. Field-cooled conditions with $H = 1000$ Oe were applied. The powder samples were enclosed in gel capsules whose small contribution to the measured susceptibility was taken into account by a temperature-independent χ_0 parameter in the data-fitting procedure.

DSC was used to determine the phase transition temperature. The samples (roughly 15 mg) were placed in sealed aluminum crucibles and measured in a Netzsch F1 Phoenix DSC. A comparable weight of Al_2O_3 was used as reference material to enhance the signal. The samples were heated from 100 K to room temperature with a rate of 5 K/min.

III. EXPERIMENTAL RESULTS AND DISCUSSION

X-ray powder diffraction revealed phase purity for almost all compounds presented in this work. Only for the samples with the highest substitution levels marginal traces of LaRuO_3 were found. The maximum substitution level can be linked to the ionic radii of the used lanthanides. The partial replacement of La^{3+} by smaller rare-earth ions causes an increasing structural stress, which finally results in the formation of impurity phases. This stress increases with decreasing ionic radius (caused by the lanthanide contraction) and, in turn, the maximum achievable substitution level was higher for the larger lanthanides. The maximum amount of rare-earth ions x in $\text{La}_{2-x}\text{R}_x\text{RuO}_5$ was found to be 0.75 for Pr, 0.6 for Nd, 0.5 for Sm, 0.3 for Gd, and 0.2 for Dy. For substitution levels beyond these values, significant amounts of other phases, mainly pyrochlores $\text{R}_2\text{Ru}_2\text{O}_7$ and LaRuO_3 , were observed. These impurities were very stable and could not be removed by further heat treatment of the sample at 1175°C , which was found to be the optimum synthesis temperature. La_2RuO_5 is only formed in a small temperature range from 1150 to 1200°C . At lower temperatures different lanthanum ruthenate compounds like $\text{La}_3\text{Ru}_3\text{O}_{11}$,^{25,26} LaRuO_3 ,²⁷ La_3RuO_7 ,²⁸ and $\text{La}_{3.5}\text{Ru}_4\text{O}_{12}$ ²⁹ were observed, which finally reacted to La_2RuO_5 at $T \geq 1150^\circ\text{C}$. Above 1200°C , the pyrochlores and other, still unidentified oxides were formed in an irreversible reaction. The Y_2TiO_5 -type ruthenates R_2RuO_5 were not observed since they only form under pressure in an oxygen-free atmosphere.

For comparison, the pure La_2RuO_5 was synthesized by the same soft-chemistry method. The cell parameters of this sample show no significant difference to the published data for a sample obtained by conventional solid-state synthesis.³⁰ We chose the structural parameters of this sample ($x = 0$) as basis set for all structural investigations and refer relative changes to them.

A. Crystal structure

As one representative example for the Rietveld refinements, Figs. 2 and 3 show the fits of the x-ray and neutron-diffraction (ND) data of $\text{La}_{1.25}\text{Pr}_{0.75}\text{RuO}_5$ recorded at 300 K. In Fig. 4, the

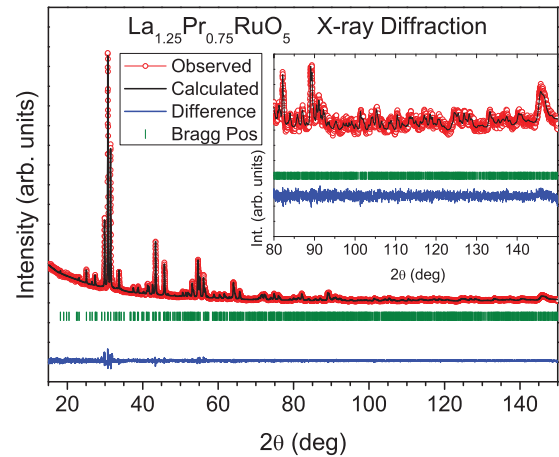


FIG. 2. (Color online) Rietveld refinement of the $\text{La}_{1.25}\text{Pr}_{0.75}\text{RuO}_5$ x-ray diffraction pattern, measured with $\text{Cu-K}\alpha_{1,2}$ radiation at room temperature. In the inset, the angular range above 80° in 2Θ is shown in more detail.

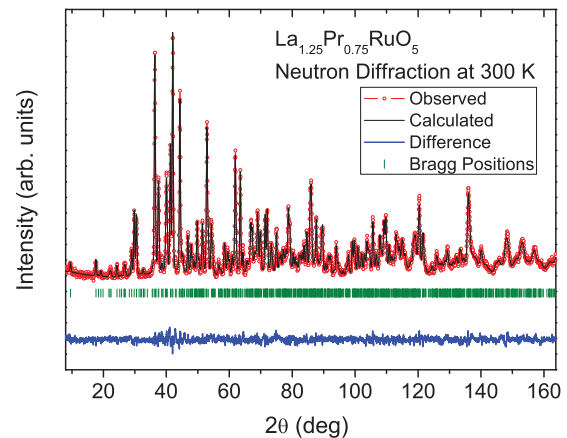


FIG. 3. (Color online) Rietveld refinement of the $\text{La}_{1.25}\text{Pr}_{0.75}\text{RuO}_5$ neutron-diffraction pattern, measured at 300 K with $\lambda = 1.494 \text{ \AA}$.

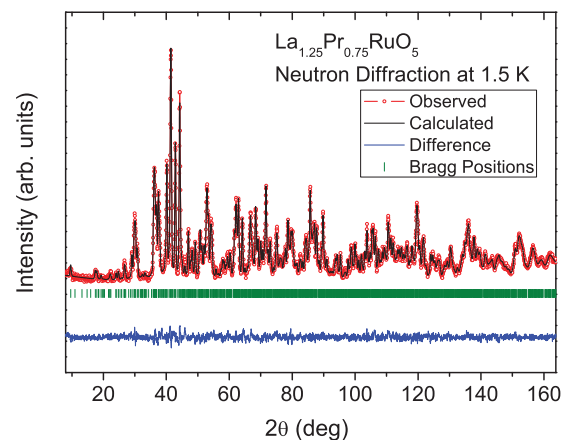


FIG. 4. (Color online) Rietveld refinement of the $\text{La}_{1.25}\text{Pr}_{0.75}\text{RuO}_5$ neutron-diffraction pattern, measured at 1.5 K with $\lambda = 1.494 \text{ \AA}$.

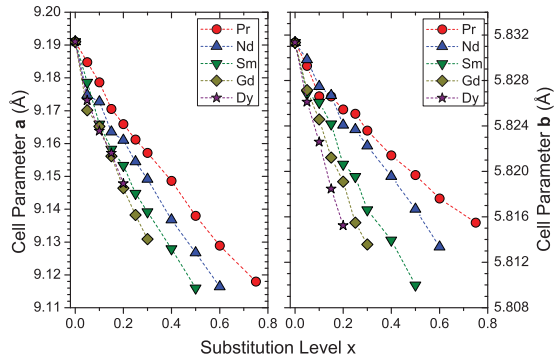


FIG. 5. (Color online) Cell parameters for $\text{La}_{2-x}\text{R}_x\text{RuO}_5$ derived from Rietveld analysis of powder XRD data at room temperature. Left: cell parameter a , right: cell parameter b . Error bars are smaller than the size of the symbols.

refinement for the ND data of the same compound recorded at 1.5 K is given. A very good agreement of measurement and fitted diffraction patterns is obvious. Numerical values obtained from the Rietveld refinements of all samples are listed in the tables in the supplementary.¹⁹

In Figs. 5 and 6. the room-temperature cell parameters of all $\text{La}_{2-x}\text{R}_x\text{RuO}_5$ samples are shown for different substitution levels x . A strong dependence on x is observed: all three axis lengths a , b , and c decline almost linearly for all rare-earth elements. The shrinkage of the three axis lengths also results in a decreasing volume of the unit cell. The effects are increasing with decreasing size of the rare-earth ion, i.e., the slopes of the curves increase in the order $\text{Pr} < \text{Nd} < \text{Sm} < \text{Gd} < \text{Dy}$. This behavior reflects the lanthanide contraction. The changes in the axis lengths can directly be linked to the maximum substitution levels mentioned above implying a structural stress limit, i.e., the limit is reached for $a \approx 9.12 \text{ \AA}$, $b \approx 5.81 \text{ \AA}$, and $c \approx 7.93 \text{ \AA}$.

The monoclinic angle β is shown on the right side of Fig. 6. The changes of the angle are small, but they also clearly depend on the rare-earth substitution. The bigger rare-earth ions Pr and Nd cause a continuous decrease of β with increasing x , the effect for Pr being stronger than for Nd. For Sm, β remains almost constant, while for the small ions Gd and Dy even

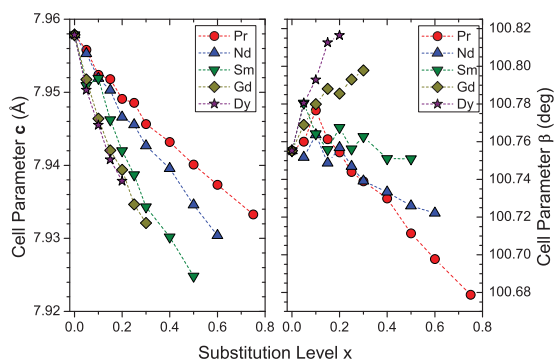


FIG. 6. (Color online) Cell parameters for $\text{La}_{2-x}\text{R}_x\text{RuO}_5$ derived from Rietveld analysis of powder XRD data at room temperature. Left: cell parameter c , right: cell parameter β . Error bars are smaller than the size of the symbols.

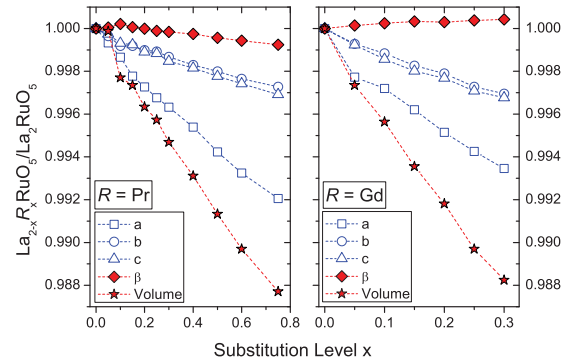


FIG. 7. (Color online) Relative change of the cell parameters for the Pr- (left) and the Gd-substituted compounds (right). The cell parameters of $\text{La}_{2-x}\text{R}_x\text{RuO}_5$ were divided by their corresponding values for La_2RuO_5 . Error bars are smaller than the size of the symbols.

enlarged angles are found. The influence of the smaller Dy is stronger than the one of Gd.

A more detailed insight in the evolution of the different cell parameters depending on x is obtained by a plot of the relative changes as presented in Fig. 7. The relative values were calculated by dividing the cell parameters of $\text{La}_{2-x}\text{R}_x\text{RuO}_5$ by their corresponding values of pure La_2RuO_5 , which makes the changes better comparable for the different lanthanides and for the cell parameters themselves. Since the behavior is similar for all rare earths, only the values for $R = \text{Pr}$ and Gd are given as examples in Fig. 7. All cell parameters change linearly with x , but a highly anisotropic behavior is observed. The axis a shows the strongest decrease with x , while the axes b and c behave almost identically and show a significantly smaller decrease than a . Since β does not change very much, the unit cell volume also decreases with x for all rare earths. Although the changes in the cell parameters are clearly significant, the relative values deviate by less than 1.3% from La_2RuO_5 , which is a surprisingly small value taking into account that substitution levels up to $x = 0.75$ were achieved.

Regarding the crystal structure and the alternating stacking of LaRuO_4 and LaO layers along the a axis the anisotropic behavior gives a first hint for the location of the substituting ions. If the smaller rare-earth ions were placed in the LaRuO_4 layer, a more or less isotropic change in structure would be expected, i.e., the relative decrease of the three axis lengths should be similar. A substitution in the LaO layers, on the other hand, is expected to predominantly shorten the interlayer distance and, therefore, mainly affect the a axis, in accordance with the experimentally observed behavior. A preferred occupation of the smaller lanthanide ions in the LaO layer is reasonable since the La-O distances in these layers are significantly shorter than those in the LaRuO_4 layer.^{1,30}

Neutron diffraction was used to investigate the distribution of the rare earths in the two distinct layers of the crystal structure. The Pr-substituted samples were measured since the scattering lengths of La (8.24 fm) and Pr (4.58 fm) are very different, while their absorption cross sections are similar.³¹ As shown in Table I, both in the high- and the low-temperature phase roughly 65–70% of the Pr^{3+} ions are placed in the LaO layers. This preferred occupation of the LaO -sites is

TABLE I. Distribution of Pr in the two different types of layers in $\text{La}_{2-x}\text{Pr}_x\text{RuO}_5$.

$\text{La}_{2-x}\text{Pr}_x\text{RuO}_5$	Pr in LaO	Pr in LaRuO_4	Sum of Pr
300 K			
$x = 0.25$	0.19(2)	0.09(2)	0.28(2)
$x = 0.75$	0.51(2)	0.27(2)	0.78(2)

in accordance with the structural data discussed above. It is reasonable to assume that for the even smaller lanthanide ions Nd^{3+} , Sm^{3+} , Gd^{3+} , and Dy^{3+} the same or even an enhanced enrichment in the LaO layers occurs. Unfortunately, these cationic orderings could not be investigated due to very similar neutron-scattering lengths and/or huge absorption cross sections.

In the triclinic *lt* structure, both La positions split into two different sites. Due to a strong correlation of the corresponding fit parameters it was not possible to refine the occupation factors of the four positions independently. Therefore, the distribution of La/Pr derived from the room-temperature ND data were fixed during the refinement of the data recorded at 1.5 K. This procedure is justified by the immobility of the rare-earth ions at room temperature and below, i.e., the cationic ordering is frozen in at these temperatures. Detailed structural data obtained from the ND data were fixed during the measurements are given in the tables in the supplementary.¹⁹

In addition to the localization of Pr, neutron diffraction was also used to study the effect of the substitution on the Ru-O bond lengths and angles. Results are discussed at the end of this section.

Due to limited beam time the neutron measurements had to be restricted to very few selected samples. Therefore, a broader choice of compositions was investigated by low-temperature x-ray diffraction at 128 K, i.e., well below the phase-transition temperature. As a main result of the low-temperature XRD data, the triclinic *lt* phase was observed for all rare-earth-substituted compounds under investigation. In Fig. 8, the cell parameters obtained from the Rietveld refinement of the low-temperature XRD data (128 K) and neutron data (1.5 K) are shown for the series of Pr-substituted samples. The values were divided by their corresponding room-temperature values for better comparability. As can be seen the results from neutron diffraction and x-ray diffraction yield almost identical values. Small deviations (especially for the *a* axis) may be due to the different temperatures (XRD 128 K, and ND 1.5 K). From Fig. 8, it is evident that the phase transition leads to an increase of *b*, a smaller increase of *a*, a barely significant decrease of *c*, and a clear decrease of β . In the triclinic *lt* phase, α is slightly decreased, while γ is increased compared to the value of 90° for both angles in the monoclinic *ht* phase (not shown in Fig. 8). It is noteworthy that the relative changes associated with the phase transition are almost independent of the substitution level *x* (see tables in the supplementary¹⁹ for numerical data).

Bond-valence-sum (BVS) calculations³² based on the Rietveld refinements of XRD and neutron-diffraction data yielded valencies that are close to the formal charge of the ions, i.e., in the LaRuO_4 layer approximately -1.9 for oxygen, $+3.0$ for lanthanum, and $+3.8$ for ruthenium. However, in

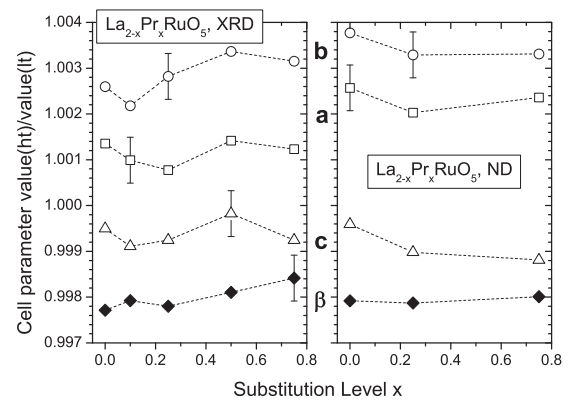


FIG. 8. Comparison of the cell parameters for the high- and low-temperature phases of $\text{La}_{2-x}\text{Pr}_x\text{RuO}_5$. Comparable room-temperature parameters have been divided by the corresponding *lt* data. Left: data from XRD, right: data from neutron diffraction.

the LaO layer, oxygen exhibits a larger negative valence of -2.4 , while the value for La is shifted to $+3.2$ caused by the shortened La-O bonds. In addition, a valence of roughly $+2.9$ is found for Pr, which is slowly decreasing for Nd, Sm, and Gd to roughly $+2.5$ and finally dropping to $+2.0$ for Dy. These valencies were found to be almost constant for all substitution degrees *x*. These findings indicate that the La-O bonds are shorter than predicted by the BVS approach while the R-O distances are too long. Apparently, structural restrictions do not allow the bonds in the (La/R)O-layers to take their preferred values.

The bond lengths, especially those between the metal ions, reveal the same dependence on the substitution level as the cell parameters. While the intralayer La-Ru distance remains almost constant, the interlayer distance between La/R and Ru decreases slightly. This effect is even more pronounced for the La-La/R distance, which is highly related to the value of the axis *a*.

As will be described later, the rare-earth substitution leads to significant changes in the physical properties of the samples, especially differences in the temperature of the magnetic ordering. It is well known that in perovskites such changes can be induced by even small variations of bond distances and/or angles. While the former can result in distortions of the metal-oxygen octahedra, which affect the energies of the *d* orbitals and may cause phenomena like orbital ordering, the latter directly influence the metal-oxygen-metal superexchange interaction due to variations in the overlap of the corresponding orbitals.³³ For this reason, a thorough inspection of the geometry of the RuO_6 octahedra and the Ru-O-Ru angles was performed. Since the atomic coordinates of oxygen can more accurately be determined by neutron than by x-ray diffraction, we only refer to the ND data in the following.

For the monoclinic high-temperature phase small changes caused by the substitution were observed. This is shown in detail in Fig. 9 for the octahedra in La_2RuO_5 and $\text{La}_{1.25}\text{Pr}_{0.75}\text{RuO}_5$. O3 and O4 are directing toward the LaO layers, while O2 is connecting the RuO_6 octahedra along the *c* axis. O5 links the RuO_6 octahedra within the *ab* plane. The O2-Ru-O2 angles are close to 178° for all samples under

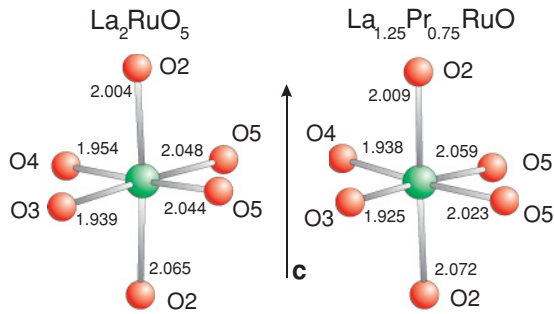


FIG. 9. (Color online) Comparison of the octahedral coordination of Ru in La_2RuO_5 and $\text{La}_{1.25}\text{Pr}_{0.75}\text{RuO}_5$ from room-temperature ND data. The oxygen atoms are labeled corresponding to the tables in the supplementary. The bond lengths are given in Å.

investigation, and also, the Ru-O bond lengths are almost constant. Ru-O5 is an exception, here, a distinct elongation of one of the bonds and simultaneous shortening of the second one is observed. Apart from this, the tilting of the RuO_6 octahedra was found to increase, when La is substituted by Pr. The angle Ru-O2-Ru (i.e., parallel to the c axis) is reduced from 152.8° for $x = 0$ to 152.3° for $x = 0.75$ in the Pr-substituted samples. This smaller bond angle results in a slightly shortened Ru-Ru distance and a small torsion of the octahedra along c , as shown in Fig. 10(a) for La_2RuO_5 (transparent) and $\text{La}_{1.25}\text{Pr}_{0.75}\text{RuO}_5$ (opaque). In the ab plane, the Ru-O5-Ru angle remains almost unchanged, while on the other hand, the O5-Ru-O5 angle decreases from 95.1° to 94.1° causing an elongation of the Ru-Ru distance by 0.015 \AA . This is illustrated in Fig. 10(b) for La_2RuO_5 (transparent) and $\text{La}_{1.25}\text{Pr}_{0.75}\text{RuO}_5$ (opaque) for the Ru-O coordination in the ab plane.

The low-temperature (1.5 K) neutron-diffraction data of the samples $\text{La}_{1.75}\text{Pr}_{0.25}\text{RuO}_5$, $\text{La}_{1.25}\text{Pr}_{0.75}\text{RuO}_5$, and $\text{La}_{1.5}\text{Nd}_{0.5}\text{RuO}_5$ reveal the same structural phase transition to the triclinic space group P1 as found for the pure La_2RuO_5 . Due to the symmetry reduction, the number of crystallographic sites doubles (indicated by the index “a” in the following), but the corresponding atoms and bonds can be discussed

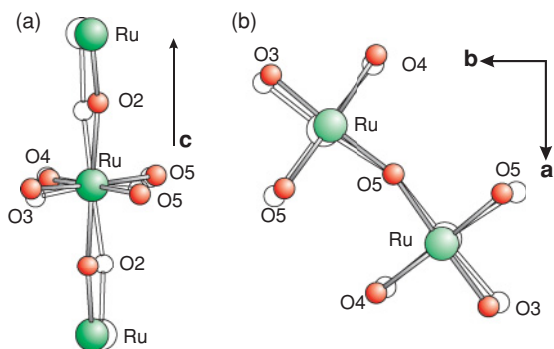


FIG. 10. (Color online) Comparison of the Ru-O2-Ru angles along the c direction (a) and of the local oxygen coordination in the ab plane (b) in La_2RuO_5 (transparent) and $\text{La}_{1.25}\text{Pr}_{0.75}\text{RuO}_5$ (opaque) from room-temperature ND data. For better comparability of changes, the central ions [Ru in (a) and O5 in (b)] were placed on the same position.

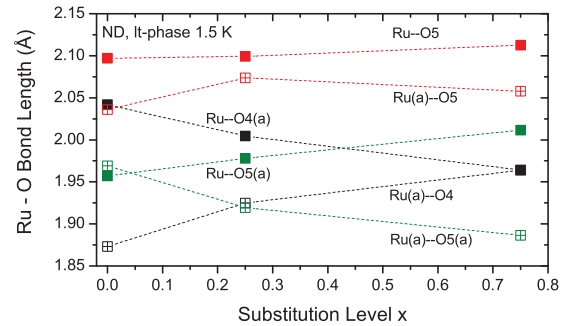


FIG. 11. (Color online) Selected Ru-O bond lengths for the It phase of $\text{La}_{2-x}\text{Pr}_x\text{RuO}_5$ derived from ND-data (1.5 K) refinements.

simultaneously. Again, similar alternating elongations and shortenings of the Ru-Ru distances are observed and the Ru-O-Ru angles show only minor changes with increasing substitution level similar to the situation in the ht phase discussed above. In contrast, we observed a deviation of two Ru-O bond lengths. First, the Ru-O bond, which is bridging the RuO_6 octahedra in the ab plane [Ru(a)-O5 and Ru(a)-O5(a)] shows an increasing dispersion of bond length with increasing x from 1.96 \AA ($x = 0$) to 1.88 \AA [$x = 0.75$, Ru(a)-O5(a)] and 2.04 \AA [$x = 0.75$, Ru-O5(a)], respectively (see Fig. 11). Second, the Ru(a)-O4 and Ru-O4(a) bonds directed toward the LaO layer act in the opposite way. The rather different values for $x = 0$ (1.88 \AA and 2.04 \AA) change to an almost identical distance of 1.96 \AA for $x = 0.75$. For comparison, the bond lengths of Ru-O5 and Ru(a)-O5 are shown in Fig. 11 representing the almost-constant values of the other Ru-O bonds for increasing x .

In summary, a variation of the shape of the RuO_6 octahedra and a reduction of the Ru-O-Ru tilting angle resulting in a torsion of the octahedra along the c axis with increasing substitution level were detected. These findings are important for the interpretation of the magnetic data presented below.

B. Magnetic properties

In combination with the structural changes discussed above, the pure La_2RuO_5 also exhibits a magnetic phase transition around 170 K, which leads to an almost complete suppression of the paramagnetic susceptibility below this temperature. This observation has been explained by a local dimerization of neighboring $\text{Ru}^{4+} S = 1$ spin moments in the ab plane in an antiferromagnetic arrangement, i.e., a spin-Peierls-like arrangement.^{6,7} An alternative explanation for the strong reduction of the magnetic susceptibility was based on an orbital-ordering effect caused by the deformation of the RuO_6 octahedra.² In this scenario, two of the Ru t_{2g} d orbitals are lowered in energy while the third is shifted to a higher energy resulting in an electronic configuration with a local moment of $S = 0$. However, this explanation could not be verified by the above mentioned DFT calculations, which support the spin-Peierls-ordering scenario.⁶ The spin pairing is connected to the structural phase transition. In the room-temperature structure, almost identical Ru-Ru bond lengths are found along the zigzag chain of RuO_6 octahedra in the ab

TABLE II. Electron configuration, ground state term symbol, and effective magnetic moments of R^{3+} from the free ion approximation.

R^{3+}	$4f^N$	$2S+1L_J$	$n_{\text{eff}} (\mu_B)$
Pr ³⁺	$4f^2$	3H_4	3.578
Nd ³⁺	$4f^3$	$^4I_{9/2}$	3.618
Sm ³⁺	$4f^5$	$^6H_{5/2}$	0.845
Gd ³⁺	$4f^7$	$^8S_{7/2}$	7.937
Dy ³⁺	$4f^9$	$^6H_{15/2}$	10.646

plane. In the low-temperature crystal structure, on the other hand, an alternating elongation/shortening of these distances is observed. One aim of the present work was to examine whether the rare-earth substitution affects or even completely suppresses this magnetic phase transition while preserving the structural changes.

For the calculation of the magnetic moments of the rare-earth ions, the free-ion approximation is a well-suited description³⁴ because the $4f$ electrons are screened by the completely filled $5s^2p^6$ shell, which is more distant from the core than the $4f$ states. Thus the magnetic moment n_{eff} can be described by

$$n_{\text{eff}} = g_J [J(J+1)]^{1/2}, \quad (1)$$

where g_J is the Lande factor

$$g_J = 1 + \frac{J(J+1) + S(S+1) - L(L+1)}{2J(J+1)}. \quad (2)$$

Variables S , L , and J are the quantum numbers for spin momentum, orbital angular momentum, and total orbital momentum obtained by the Hund's rules. In Table II, the magnetic moments of the different trivalent rare-earth ions used for substitution are listed together with the $4f^N$ electron configuration and the ground-state term symbol $2S+1L_J$.

In the top frame of Fig. 12, the magnetic susceptibilities $\chi(T)$ of La_2RuO_5 and $\text{La}_{1.9}\text{R}_{0.1}\text{RuO}_5$ for $H = 1$ kOe are depicted. The results for $\text{La}_{1.9}\text{R}_{0.1}\text{RuO}_5$ are dominated by the additional magnetic moments of the rare earths. All curves possess a clear step at the transition temperature with a reduced susceptibility. This reduction is of similar magnitude for all samples. In the lower frame, the inverse magnetic susceptibility $1/\chi(T)$ shows the influence of the magnetic lanthanide ions more clearly. The higher the value of $1/\chi$ below 170 K the smaller is the additional magnetic moment of the rare-earth ion. The order of reduction is $\text{La} > \text{Sm} > \text{Pr} \geq \text{Nd} > \text{Gd} > \text{Dy}$, which reflects the values listed in Table II.

For a quantitative analysis, a fit of the inverse susceptibility in the temperature range 200 to 300 K with a Curie-Weiss law was performed,

$$\chi(T) = \frac{C}{T - \Theta_{\text{CW}}} + \chi_0. \quad (3)$$

The temperature-independent contribution χ_0 accounts for a possible van Vleck paramagnetic contribution, the moment of the sample holder as well as the diamagnetic contribution of the core electrons. The susceptibility χ_0 was found to be in a negligible range of 10^{-5} emu/mol for all samples and is

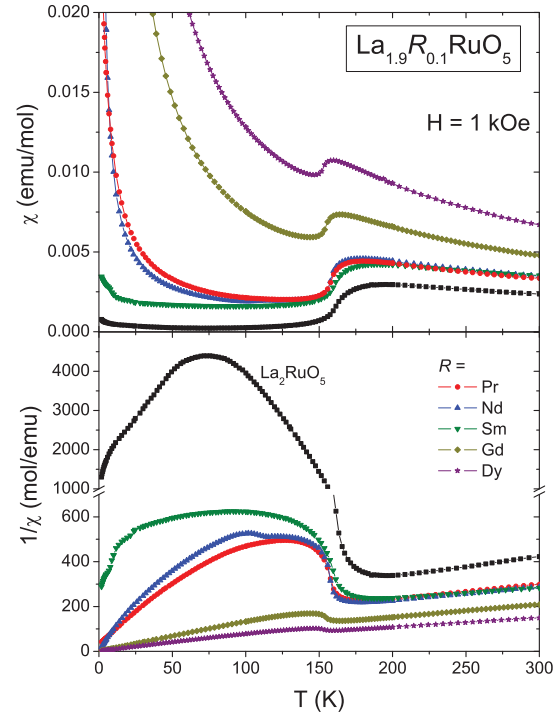


FIG. 12. (Color online) Upper graph: magnetic susceptibility χ of La_2RuO_5 and $\text{La}_{1.9}\text{R}_{0.1}\text{RuO}_5$ at $H = 1$ kOe. Lower graph: inverse magnetic susceptibility $1/\chi$.

therefore not discussed here. The values for n_{eff} derived from C are shown in Fig. 13 for each lanthanide ion. The solid lines represent the calculated $n_{\text{eff, total}}$ according to a summation of the Ru^{4+} and the R^{3+} magnetic moments

$$n_{\text{eff, total}} = \sqrt{n_{\text{eff, Ru}}^2 + x n_{\text{eff, R}}^2}, \quad (4)$$

where x represents the substitution level. With this model, an excellent agreement is achieved as can be seen from Fig. 13. Only the pure sample La_2RuO_5 shows a slightly increased moment of $2.91\mu_B$ compared to the theoretical $2.83\mu_B$ for

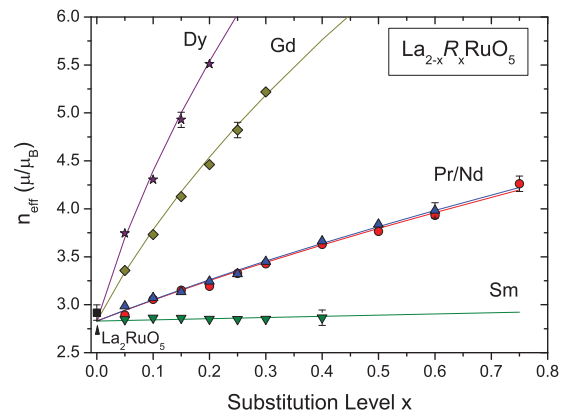


FIG. 13. (Color online) Effective magnetic moments in Bohr magnetons from Curie-Weiss fits of $1/\chi$ in the temperature range 200–300 K. The full lines represent the summation according to Eq. (4) of the Ru^{4+} and R^{3+} spin moments calculated from the spin-only and free-ion approximations, respectively.

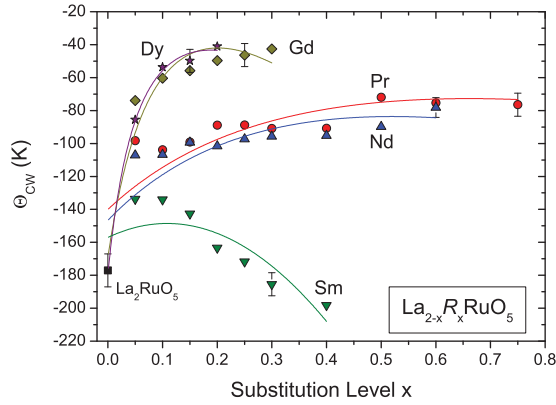


FIG. 14. (Color online) Curie-Weiss temperatures Θ_{CW} from the fit of $1/\chi$ in the temperature range 200–300 K. The lines represent Θ_{CW} values calculated with Eq. (5).

Ru^{4+} obtained from the spin-only approximation. However, this deviation is still in the range of the error bars, which are of $\pm 0.1\mu_B$ due to the small temperature range for which the Curie-Weiss law is applicable in the measurement (200–300 K).

In Fig. 14, the Curie-Weiss temperatures Θ_{CW} derived from the same fits are shown. The negative signs indicate an antiferromagnetic interaction in the paramagnetic high-temperature phase. The strength of this interaction is represented by the absolute value of Θ_{CW} . The Curie-Weiss temperature is reduced from -177 K for La_2RuO_5 by the insertion of the rare-earth ions. Clearly, the changes in the Curie-Weiss temperatures depend on the magnetic moment of the substituting rare-earth ion. Dysprosium with the highest moment leads to the strongest change in Θ_{CW} with values ranging from roughly -85 K at $x = 0.05$ to -40 K at $x = 0.2$. The Gd samples, which possess a comparable magnetic moment, exhibit a very similar behavior. Pr and Nd show almost identical magnetic moments and also the Curie-Weiss temperatures of the Pr- and Nd-substituted compounds are very similar for all substitution values x . Starting from -110 K for $x = 0.05$, Θ_{CW} declines slowly to around -80 K for $x = 0.75$. A very interesting exception are the Sm-containing compounds, which reveal a different behavior with Θ_{CW} increasing from -150 to about -200 K for $La_{1.6}Sm_{0.4}RuO_5$ (see Fig. 14).

Theoretical Θ_{CW} values can be calculated by Eq. (5), which is valid for an antiferromagnetically interacting system consisting of two different magnetic sublattices of atoms A (Ru^{4+}) and B (R^{3+}).³⁵

$$\Theta_{CW} = \frac{2\lambda_{AB}C_A C_B - \lambda_{AA}C_A^2 - \lambda_{BB}C_B^2}{C_A + C_B}. \quad (5)$$

In this equation, C_A and C_B are the Curie constants of Ru^{4+} and R^{3+} . Parameters λ_{AA} and λ_{BB} represent the fitting parameters of the two sublattices and λ_{AB} is the effective coupling between the two systems. The interaction strengths W , according to Goodenough,³⁵ in and between the lattices could be calculated from the fitting parameters, starting with $\lambda_{AB} = -W_{AB}$. For the two different lattices, the internal coupling values are calculated by $W_{AA} = W_{AB} \times \lambda_{AA}$ and $W_{BB} = W_{AB} \times \lambda_{BB}$, respectively.

The Curie constants C_A and C_B were obtained from the theoretical effective magnetic moments of R^{3+} and Ru^{4+} ions [Eq. (4)]. The parameters λ_{AB} , λ_{AA} , and λ_{BB} were obtained from a least-square fitting. As a starting point for λ_{AA} (i.e., the interaction of the Ru-moments) the value for undoped La_2RuO_5 was used, which can be derived from $\Theta_{CW} = -\lambda_{AA} \times C_A$. The calculated data for the Curie-Weiss temperatures according to Eq. (5) are drawn in Fig. 14 as solid lines using the same colors as for the measured values (shown as symbols). In general, a satisfying agreement between the experimental Θ_{CW} values and the calculated ones is observed. All coupling strengths W possess a negative sign indicating an antiferromagnetic interaction and for the Pr, Nd, Gd, and Dy substituted compounds, an ascending order of absolute values $W_{AB} \ll W_{BB} < W_{AA}$ was found. In contrast, for the Sm-containing samples, the Sm-Sm interactions are strongly dominating ($W_{AB} \ll W_{AA} \ll W_{BB}$), which leads to the decrease of Θ_{CW} values and the appearance of a maximum at very low substitution levels. In summary, the weakest interaction for all compounds was found between the two sublattices and the strongest coupling was obtained within the Ru^{4+} sublattice (except for Sm) in accordance with the observed Ru-spin dimerisation below approximately 170 K. Crystal-field effects (especially for Pr and Nd³⁶) and the different nature of the interaction between the two crystallographic R sites and the Ru^{4+} sublattice may have to be regarded for a more detailed explanation of the Θ_{CW} behavior. The crystal-field effects are reflected by the values of λ_{AA} , which are deviating at $x = 0$ for the Pr-, Nd-, and Sm-substituted compounds, the strongest observed for Pr followed by Nd and the weakest for Sm.

The quality of the fit may be improved by a more complicated model, which accounts for the two $R-Ru^{4+}$ exchange-interaction terms for each site, which have to be weighted since their occupancies are different as shown with the data from neutron diffraction. In the case of Sm-substituted samples, the obtained results should be treated with caution since the magnetic moment of Sm^{3+} is small (see Table II) and n_{eff} is temperature dependent as a result from the energetically close $4f$ multiplet levels.³⁴

From the above discussed results it can be concluded that the influence of the rare-earth ions, which are preferably occupying the LaO intermediate layer, on the Ru-Ru dimerization is very small. The reduction of the Curie-Weiss temperature with higher substitution level and different R^{3+} moments and the observed interaction strengths are confirming the assumption of an only weak interaction between the two sublattices. A similar situation was recently found for $R_{2/3}Cu_3Ti_4O_{12}$,³⁷ which also can be considered as consisting of two nearly independent spin systems.

C. Determination of the phase transition temperature from synchrotron x-ray diffraction, DSC, and magnetic-susceptibility data

The phase transition of pure La_2RuO_5 was investigated with synchrotron x-ray diffraction. The contributions of the monoclinic ht and the triclinic lt phases were determined for temperatures between 50 and 300 K. Starting at room temperature the sample was cooled down and roughly every

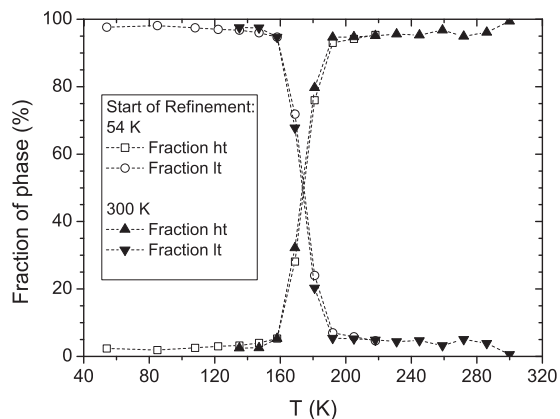


FIG. 15. Quantitative phase analysis of La_2RuO_5 depending on temperature. Fractions of ht and lt phase were calculated from synchrotron-diffraction data for a stepwise cooling from 300 to 54 K.

10 K a diffraction pattern was recorded. Afterward, the sample was heated up again to check for a possible hysteresis of the transition. The fractions of the ht and lt phases were calculated from Rietveld refinement at each temperature step and the result is shown in Fig. 15 for the patterns obtained from the cooling cycle. In the refinements, the scaling factors, the cell parameters, and the overall displacement parameter were allowed to vary, while the atomic positions were kept fixed. The obtained result at a given temperature was used as starting point for the refinement of the next temperature step. To check whether or not this procedure leads to reliable results, we tried both directions, i.e., starting from the highest temperature going down and starting from the lowest temperature going up. Both sets of refinements yielded almost identical compositions as shown in Fig. 15. Obviously, the phase transition itself is very broad, ranging over roughly 40 K. In this temperature interval, the diffraction patterns can be described by a mixture of both phases. At higher or lower temperatures only the ht or lt phase is present. A similar result was reported by Khalifah *et al.* on basis of neutron-diffraction data.² These authors found a similar transition range but reported a slightly lower transition temperature of 160 K. Comparing these results with the heating cycle (not shown in Fig. 15), no hysteresis was observed. Therefore, the phase transition is fully reversible without any dissipative character. Moreover, the DSC data, discussed in detail below, support this finding since only small differences (less than 2 K) between the heating and cooling measurements were observed.

The influence of the substitution on the phase transition was investigated by two methods, namely, magnetic measurements and differential scanning calorimetry. For the determination of the transition temperature from the susceptibility data, the paramagnetic contribution of the ht phase was calculated using the above obtained values for C , Θ_{CW} , and χ_0 , and subtracted from the $1/\chi$ data. The obtained results are shown in Fig. 16 for selected Pr-substituted compounds. The Néel temperature (T_N) was taken from the onset, i.e., the intersection point of the tangent of the $1/\chi$ curve with the temperature axis. A remarkable temperature change can be observed in Fig. 16. The onsets of the curves are shifted toward lower temperatures

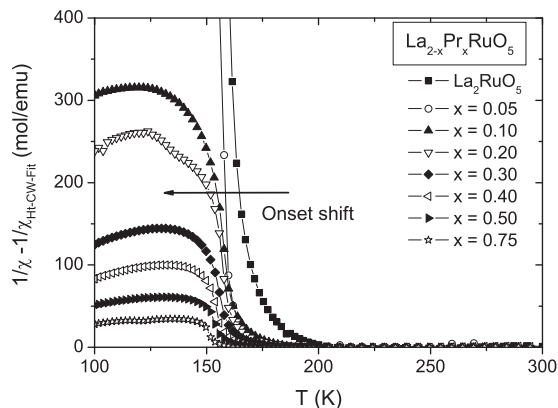


FIG. 16. Inverse magnetic susceptibility of the Pr-substituted samples after subtraction of the high-temperature moment deduced from Curie-Weiss fits. See text for details.

with increasing rare-earth substitution level. Numerical values are shown in Fig. 18 and discussed below.

Transition-temperature data were also derived from DSC measurements by slowly heating the samples from 100 K to room temperature. In Fig. 17, a typical DSC measurement is depicted. The small sharp peaks below the transition temperature are instrumental artifacts. In analogy to the magnetic measurements, the onset temperature for the transition was determined as shown in Fig. 17. As a second characteristic, the temperature of the DSC peak was used. The transition leads to an endothermic signal caused by the breaking up of the Ru-Ru dimers during heating.

In Fig. 18, the transition temperatures derived from the susceptibility data and the DSC measurements are shown for the Pr- (left) and the Nd- (right) substituted compounds. The results from the different methods agree very well with deviations of only a few Kelvin. The agreement is slightly better for Nd than for Pr. As a general trend, we observed a linear shift of the transition temperatures to lower values with increasing substitution level x .

The transition temperatures of the Sm, Gd, and Dy compounds could not be obtained from DSC data because their

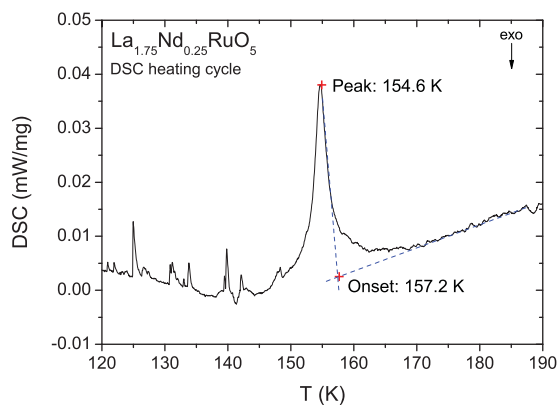


FIG. 17. (Color online) DSC curve from the heating of $\text{La}_{1.75}\text{Nd}_{0.25}\text{RuO}_5$. The onset temperature was taken from the intersection of the two blue dashed tangents.

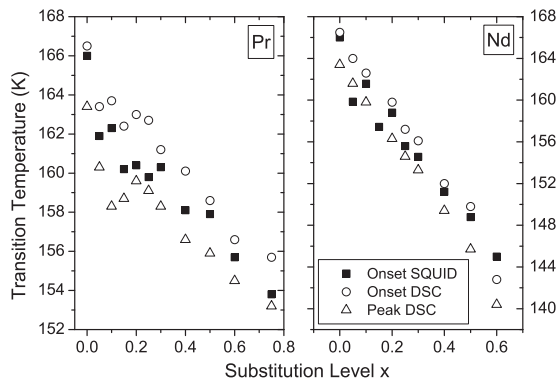


FIG. 18. Comparison of the transition temperatures obtained by DSC and magnetic measurements for the Pr- and Nd-substitution series.

values were below the measurement range of the instrument. Thus, only the magnetization results are shown in Fig. 19 for all compounds investigated. Comparing the temperature changes from Fig. 19 with the structural data of the unit cell axis lengths a depicted in Fig. 5, a remarkably similar behavior is found. Obviously, the decrease of T_N is directly correlated to the structural compression, which confirms the strong linkage between the structural and magnetic phase transitions. On the other hand, no significant influence of the magnetic moments of the substituting rare earths on the temperature change of T_N was detected. This again proves the weakly coupled magnetic moments of Ru^{4+} and the R^{3+} ions.

The Néel temperatures shown in Figs. 18 and 19 can be compared with the values of $|\Theta_{\text{CW}}|$ from the Curie-Weiss fit of the inverse susceptibility. In La_2RuO_5 and the Sm-substituted compounds, T_N and $|\Theta_{\text{CW}}|$ are comparable (around 170 K). The Pr- and Nd-substituted compounds show $|\Theta_{\text{CW}}|$ values that are roughly half of T_N . For Gd and Dy, the ratio of $T_N/|\Theta_{\text{CW}}|$ is even less than one third. Although these deviations are high, they do not provide a proof for magnetic frustration, which is usually indicated by a considerably higher ratio (at least a factor of ten³⁸).

From the above given results it can be summarized that the phase transition is not considerably influenced by the

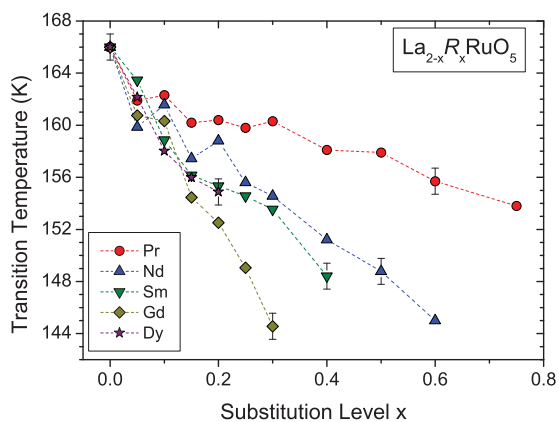


FIG. 19. (Color online) Transition temperatures T_N obtained from magnetic susceptibility data for $\text{La}_{2-x}\text{R}_x\text{RuO}_5$.

magnetic moments of the lanthanides. In contrast, the evolution of the transition temperature is obviously directly correlated to the structural changes caused by the smaller radii of the rare-earth ions. It is to be noted that the effect of the substitution turned out to be opposite to what we originally expected. The incorporation of the smaller R ions leads to a reduction of the cell parameters. Therefore, the distance between the paramagnetic Ru^{4+} centers in the a direction becomes shorter, while the intralayer distances in the LaRuO_4 layers remain merely constant. One would expect that this shorter distance results in a stronger interaction and, in turn, to an increase of the magnitude of T_N . In contrast, T_N and also $|\Theta_{\text{CW}}|$ decrease, revealing a weaker antiferromagnetic interaction. This reduced antiferromagnetic coupling may partly be caused by the increasing deformation of the RuO_6 octahedra with increasing x . Probably more important are the observed changes in the Ru-O-Ru angles. According to Goodenough³⁹ and Kanamori³³ a Ru-O-Ru angle of 180° (corner sharing octahedra of d^4 transition metals) leads to an antiferromagnetic interaction while a 90° angle (as found in edge-sharing octahedra) results in a ferromagnetic coupling. As discussed in detail in Sec. III A, we found a small decrease of the Ru-O-Ru angles along c as a result of the introduction of the smaller rare-earth ions. This smaller bond angle is expected to result in a weakening of the antiferromagnetic coupling parallel to this crystallographic direction. However, the observed reduction of the tilting angle is maybe too small to explain the lower transition temperatures only by the superexchange mechanism. Another possible explanation comes from the unit cell volume contraction with increasing x itself. The contraction causes an enhanced overlap of orbitals that results in a broadening of the electron bands near the Fermi level. This broadening is leading to a less localized nature of the electrons,⁴⁰ which in turn causes a weakening of the antiferromagnetic ordering and a decrease of T_N .

IV. SUMMARY AND CONCLUSIONS

Substitution with various rare-earth elements was achieved in La_2RuO_5 by a soft-chemistry synthesis route. The obtained samples can be described by the formula $\text{La}_{2-x}\text{R}_x\text{RuO}_5$ ($R = \text{Pr, Nd, Sm, Gd, and Dy}$). Depending on the ionic radii of the lanthanide ions different maximum substitution levels were observed. The maximum value of x is 0.75 for Pr and is declining to 0.2 for Dy. This is a direct consequence of the lanthanide contraction. The single-phase polycrystalline samples were investigated by x-ray diffraction in combination with Rietveld refinement. All compounds show a structural phase transition from a monoclinic ht to a triclinic lt modification. The high temperature and low temperature phase symmetry are the same as in pure La_2RuO_5 , but the unit cell volume decreases due to the shortening of the axis lengths. This effect is anisotropic and is mainly caused by the reduction of the axis a , which is directed perpendicular to the layering in the compound. Neutron diffraction of $\text{La}_{1.75}\text{Pr}_{0.25}\text{RuO}_5$ and $\text{La}_{1.25}\text{Pr}_{0.75}\text{RuO}_5$ yielded a preferred occupation of the rare-earth ions in the intermediate LaO layers, explaining the anisotropic structural changes. Magnetic-susceptibility data additionally indicate the

presence of two weakly interacting magnetic sublattices. The first sublattice is formed by the spins of the Ru^{4+} ions, which show a spin-Peierls-like dimerization at temperatures below 170 K in all investigated samples. In addition, a decrease of the transition temperature was observed depending on the used rare-earth element and the substitution level x . The second magnetic sublattice consists of the paramagnetic R^{3+} ions.

For the Pr- and Nd-substituted compounds the transition (Néel) temperatures determined by SQUID and DSC measurements are very similar.

From the reduction of the cell parameter values and, in turn, shorter distances of the Ru^{4+} ions, a stronger magnetic interaction was expected. Instead, we observed a decrease of the absolute value of the Curie-Weiss temperature and of the Néel temperature indicating a weakened interaction. Moreover, the effect on the dimerization temperature is solely caused by the changes in the crystal structure and not by additional magnetic moments of R^{3+} . The deformation of the RuO_6 octahedra and an increasing of the octahedral tilting could be the causes for the weakening of the antiferromagnetic interaction between the Ru ions. In an alternative explanation, the unit cell volume contraction and the resulting broadening of the electronic bands could decrease the transition temperatures.

This study provides a detailed investigation of the composition-structure-property relation in the layered perovskite-related oxide La_2RuO_5 . By small changes in crystal structure, the magnetic properties and especially the transition temperature are significantly modified. A very promising way of more directly affecting the Ru-Ru interaction is the substitution of Ru by other transition metals. The corresponding work is currently under progress and results will be reported in the near future.

ACKNOWLEDGMENTS

The authors gratefully acknowledge the DFG (SFB 484) for financial support, HASYLAB for the allocated beamtime, Dana Vieweg for SQUID measurements, and the chair of Experimental Physics 6 (University of Augsburg) for the opportunity to make the low-temperature XRD measurements. This work is partly based on experiments performed at the Swiss spallation neutron source SINQ, Paul Scherrer Institute, Villigen, Switzerland. Technical assistance by Denis Sheptyakov is gratefully acknowledged. Additional thanks are to Volker Eyert for the fruitful discussion about DFT calculations.

*stefan.riegg@physik.uni-augsburg.de

¹P. Boullay, D. Mercurio, A. Bencan, A. Meden, G. Drazic, and M. Kosec, *J. Solid State Chem.* **170**, 294 (2003).

²P. Khalifah, R. Osborn, Q. Huang, H. W. Zandbergen, R. Jin, Y. Liu, D. Mandrus, and R. J. Cava, *Science* **297**, 2237 (2002).

³S. K. Malik, D. C. Kundaliya, and R. D. Kale, *Solid State Commun.* **135**, 166 (2005).

⁴D. I. Khomskii and T. Mizokawa, *Phys. Rev. Lett.* **94**, 156402 (2005).

⁵Hua Wu, Z. Hu, T. Burnus, J. D. Denlinger, P. G. Khalifah, D. G. Mandrus, L.-Y. Jang, H. H. Hsieh, A. Tanaka, K. S. Liang, J. W. Allen, R. J. Cava, D. I. Khomskii, and L. H. Tjeng, *Phys. Rev. Lett.* **96**, 256402 (2006).

⁶V. Eyert and S. G. Ebbinghaus, *Prog. Solid State Chem.* **35**, 433 (2007).

⁷V. Eyert, S. G. Ebbinghaus, and T. Kopp, *Phys. Rev. Lett.* **96**, 256401 (2006).

⁸S. J. Blundell, T. Lancaster, P. J. Baker, W. Hayes, F. L. Pratt, T. Atake, D. S. Rana, and S. K. Malik, *Phys. Rev. B* **77**, 094424 (2008).

⁹G. Cao, S. McCall, Z. X. Zhou, C. S. Alexander, J. E. Crow, R. P. Guertin, and C. H. Mielke, *Phys. Rev. B* **63**, 144427 (2001).

¹⁰L. L. Kochergina, O. I. Kondratov, Yu. S. Shorikov, V. V. Fomichev, and K. I. Petrov, *Russ. J. Inor. Chem.* **27**, 1137 (1982).

¹¹S. Dixon, J. Marr, E. E. Lachowski, J. A. Gard, and F. P. Glasser, *Mater. Res. Bull.* **15**, 1811 (1980).

¹²W. G. Mumme and A. D. Wadsley, *Acta Crystallogr. Sect. B* **24**, 1327 (1968).

¹³T. Yamamoto, R. Kanno, Y. Takeda, O. Yamamoto, Y. Kawamoto, and M. Takano, *J. Solid State Chem.* **109**, 372 (1994).

¹⁴B. J. Kennedy and T. Vogt, *J. Solid State Chem.* **126**, 261 (1996).

¹⁵A. Douy and P. Odier, *Mater. Res. Bull.* **24**, 1119 (1989).

¹⁶S. G. Ebbinghaus, S. Riegg, T. Götzfried, and A. Reller, *Eur. Phys. J. Special Topic* **180**, 91 (2010).

¹⁷M. P. Pechini, U. S. Patent 3330697 (1967).

¹⁸H. M. Rietveld, *J. Appl. Crystallogr.* **2**, 65 (1969).

¹⁹See Supplemental Material at <http://link.aps.org/supplemental/10.1103/PhysRevB.84.014403> for detailed information of cell parameters, atomic coordinates, and isotropic displacement values for $\text{La}_{2-x}\text{R}_x\text{RuO}_5$.

²⁰J. Rodriguez-Carvajal, *Physica B* **192**, 55 (1993).

²¹H. H. Landolt and R. Börnstein, *Zahlenwerte und Funktionen aus Physik, Chemie, Astronomie, Geophysik und Technik* (Springer, Berlin, Heidelberg, 1964), IV. Band: Technik, Teil 2b.

²²P. Fischer, G. Frey, M. Koch, M. Könnecke, V. Pomjakushin, J. Schefer, R. Thut, N. Schlumpf, R. Bürge, U. Greuter, S. Bondt, and E. Berruyer, *Physica B* **276–278**, 146 (2000).

²³M. Knapp, C. Baetz, H. Ehrenberg, and H. Fuess, *J. Synchrotron Radiat.* **11**, 328 (2004).

²⁴M. Knapp, V. Joco, C. Baetz, H. H. Brecht, A. Berghaeuser, H. Ehrenberg, H. von Seggern, and H. Fuess, *Nucl. Instrum. Methods Phys. Res., Sect. A* **521**, 565 (2004).

²⁵F. Abraham, J. Trehoux, and D. Thomas, *Mater. Res. Bull.* **13**, 805 (1978).

²⁶A. Cotton and C. E. Rice, *J. Solid State Chem.* **25**, 137 (1978).

²⁷R. J. Bouchard and J. F. Weiher, *J. Solid State Chem.* **4**, 80 (1972).

²⁸P. Khalifah, Q. Huang, J. W. Lynn, R. W. Erwin, and R. J. Cava, *Mater. Res. Bull.* **35**, 1 (2000).

²⁹F. Abraham, J. Trehoux, and D. Thomas, *J. Solid State Chem.* **32**, 151 (1980).

³⁰S. G. Ebbinghaus, *Acta Crystallogr. Sect. C* **61**, i96 (2005).

- ³¹Neutron News **3**, 29 (1992).
- ³²I. D. Brown and D. Altermatt, *Acta Crystallogr. Sect. B* **41**, 244 (1985).
- ³³J. Kanamori, *J. Phys. Chem. Solids* **10**, 87 (1959).
- ³⁴H. Lueken, *Magnetochemie* (Teubner, Stuttgart, Leipzig, 1999).
- ³⁵J. B. Goodenough, *Magnetism and the Chemical Bond* (Interscience, Wiley, New York, London, 1963).
- ³⁶W. G. Penney and R. Schlapp, *Phys. Rev.* **41**, 194 (1932).
- ³⁷A. Dittl, S. Krohns, J. Sebald, F. Schrettle, M. Hemmida, H.-A. Krug von Nidda, S. Riegg, A. Reller, S. G. Ebbinghaus, and A. Loidl, *Eur. Phys. J. B* **79**, 391 (2011).
- ³⁸S. G. Ebbinghaus, E.-W. Scheidt, and T. Götzfried, *Phys. Rev. B* **75**, 144414 (2007).
- ³⁹J. B. Goodenough and A. L. Loeb, *Phys. Rev.* **98**, 391 (1955).
- ⁴⁰R. Hoffmann, *Angew. Chem., Int. Ed. Engl.* **26**, 846 (1987).